

Special  
Collection

# Phosphorus-Functionalized Graphene for Lithium-Ion Capacitors with Improved Power and Cyclability

Gelinas Moreno-Fernández,<sup>[a]</sup> Miguel Granados-Moreno,<sup>[a]</sup> Juan Luis Gómez-Urbano,<sup>[a, b]</sup> and Daniel Carriazo<sup>\*,[a, c]</sup>

Herein, we report an easy approach for the preparation of graphene-based materials suitable as electrodes for lithium-ion capacitors (LICs). To the best of our knowledge, this is the first time that phosphorus-functionalized graphene oxide (rGO800-P) is used as negative (battery-type) electrode in LICs technology. An activated carbon derived from the pyrolysis of graphene-carbon composite served as positive (capacitor-type) electrode. While phosphorus functionalization on the negative electrode enables fast Li<sup>+</sup> kinetics during insertion/extraction

processes, the flat-shaped morphology, large surface area and proper pore size distribution of the positive electrode enhance the double-layer formation. Full LICs optimization, oversizing the negative electrode allows operating in the extended voltage window of 1.5–4.5 V delivering high energy and power values (91 Wh kg<sup>-1</sup><sub>AM</sub> at 145 W kg<sup>-1</sup><sub>AM</sub> and 33 Wh kg<sup>-1</sup><sub>AM</sub> at 26,000 W kg<sup>-1</sup><sub>AM</sub>) without compromising the cycling performance (76% capacitance retention after 10,000 cycles).

## 1. Introduction

The huge amount of energy demanded nowadays by our society requires the development of safer and more environmentally friendly energy storage systems. In the last three decades, lithium-ion batteries (LIBs) have dominated the worldwide energy storage market due to their high energy density (150–200 Wh kg<sup>-1</sup>), low-self discharge and high cell voltage. Nevertheless, their low power density (1 kW kg<sup>-1</sup>) and poor cycling stability (<4,000 cycles) make them unsuitable for a certain number of applications.<sup>[1–3]</sup> Conversely, supercapacitors (SC), showing low energy densities (<10 Wh kg<sup>-1</sup>), are the preferred choice when high power (>10 kW kg<sup>-1</sup>) and almost unlimited lifespan are demanded.<sup>[4,5]</sup> Lithium-ion capacitors (LICs) have emerged as good candidates to overcome the aforementioned power and energy limitations of LIBs and SCs. They combine a capacitor-type electrode (positive electrode)

with a battery-type (negative electrode) in the same cell. In the capacitor-type the energy is physically stored by fast adsorption/desorption of the electrolyte anions on the surface of the electrode. Conversely, in the battery-type the energy is chemically stored by Li<sup>+</sup> intercalation/de-intercalation via faradaic reactions into the bulk of the electrode. Such configuration provides energy densities higher than that of SCs and power rates and cycling performances better than that of LIBs.<sup>[6–8]</sup>

In the last years, dual carbon LICs (DC-LICs), in which both electrodes consist of carbon-based materials, have gained considerable attention due to the absence of scarce and expensive metals and their excellent long-term cycling stability and outstanding power density.<sup>[9,10]</sup> Among the different carbonaceous materials reported in literature, graphene has demonstrated to be one of the most promising materials for energy storage in LICs technology. Graphene-based materials showing excellent electrical conductivity and charge transport mobility, large specific surface area, as well as chemical and mechanical stability can be used either as active material for the negative or positive electrode.<sup>[6,11]</sup> Nevertheless, considering the different charge-storage mechanisms and electrode kinetics governing each electrode, an individual optimization has to be carefully made in order to assure an efficient performance of the final device.

The main challenge of this technology is the optimization of the battery-type electrode, to increase its power performance and cycling stability. Although graphite is the most used anode in dual carbon LICs, the slow intercalation of lithium in its structure, directly related to its morphology and particle size, may limit their performance at high current rates.<sup>[12]</sup> So, alternative materials such as hard carbon, soft carbon or graphene have emerged as good candidates to replace graphite.<sup>[12]</sup> Especially, the bidimensional structure of graphene favours the reaction with lithium and its superior electron carrier mobility, can fasten kinetics during the insertion/

[a] Dr. G. Moreno-Fernández, M. Granados-Moreno, J. L. Gómez-Urbano, Dr. D. Carriazo  
Centre for Cooperative Research on Alternative Energies (CIC energiGUNE)  
Basque Research and Technology Alliance (BRTA)  
Alava Technology Park, Albert Einstein 48, 01510 Vitoria-Gasteiz, Spain  
E-mail: dcarriazo@cicenergigune.com

[b] J. L. Gómez-Urbano  
Universidad del País Vasco, UPV/EHU  
48080 Bilbao, Spain

[c] Dr. D. Carriazo  
IKERBASQUE, Basque Foundation for Science  
48013 Bilbao, Spain

Supporting information for this article is available on the WWW under <https://doi.org/10.1002/batt.202000247>

An invited contribution to a Special Collection dedicated to Metal-Ion Hybrid Supercapacitors

© 2020 The Authors. Batteries & Supercaps published by Wiley-VCH GmbH. This is an open access article under the terms of the Creative Commons Attribution Non-Commercial NoDerivs License, which permits use and distribution in any medium, provided the original work is properly cited, the use is non-commercial and no modifications or adaptations are made.

extraction processes.<sup>[11]</sup> Additionally, the functionalization of this bidimensional structure can further improve the power performance.<sup>[13–15]</sup> Particularly, it has been proved that phosphorus doping or functionalization induces topological defects with higher electron donating ability than carbon (C), which speeds the kinetics for Li<sup>+</sup> storage and transportation.<sup>[16–19]</sup>

Regarding the optimization of the capacitor-type electrode, the major goal is to increase their charge storage capacity. Porous carbons, such as activated carbons (AC), are the preferred choice, since, as widely known, large specific surface areas (SSA) and tailored pore size distributions (PSD) can allow better adsorption/desorption of a larger number of ions on the cathode surface, leading to higher specific capacitances.<sup>[20]</sup> Thus, carbons derived from the pyrolysis of polymers, such as phenolic resins, have been pointed out as promising candidates since their structure and pore size distribution can be easily tuned to maximize ion adsorption according to the electrolyte selected.<sup>[21,22]</sup> Nevertheless, the electronic properties can be somehow worsened upon the activation process. In this context, the design of composites, which may combine high electronic conductivities and large specific surface areas, to maximize capacitance at high current rates, is of paramount importance in these technologies.<sup>[23]</sup>

In the present work, graphene-based dual-carbon LICs have been developed. Reduced graphene oxide functionalized with phosphorus, showing excellent capacity performance of 316 mAh g<sup>-1</sup> at 1 C, was used as battery-type material for the first time in LICs technology. Activated carbon derived from the pyrolysis of graphene oxide–phenolic resin composite, showing outstanding capacity values of 136 mAh g<sup>-1</sup> at 0.25 A g<sup>-1</sup> was used as capacitive-type material. Optimized LICs were assembled to deliver the maximum energy and power performance under safe conditions. It was found that 3:1 negative to positive electrode mass ratio allows the smooth operation of the cell in the 1.5–4.5 V voltage range, preventing lithium plating and delivering high gravimetric energy and power densities (91 Wh kg<sup>-1</sup><sub>AM</sub> at 145 W kg<sup>-1</sup><sub>AM</sub> and 33 Wh kg<sup>-1</sup><sub>AM</sub> at 26,000 W kg<sup>-1</sup><sub>AM</sub>) and an excellent cycling stability showing 76% capacitance retention after 10,000 cycles.

## Experimental Section

### Phosphorus-Functionalized Graphene and Activated Carbon Synthesis

Phosphorus functionalized graphene oxide was synthesized following the procedure reported in our previous work.<sup>[24]</sup> Briefly, a homogenous suspension was prepared by stirring 50 mL of commercial graphene oxide (Graphenea, 4 mg mL<sup>-1</sup>) and 200 μL of concentrated phosphoric acid. The mixture was transferred into a closed container to an oven at 80 °C for 18 h. A subsequent freeze/freezing-drying process was carried out for 3 days to get the dried material. A thermal treatment at 800 °C for 1 h in a tubular oven under dynamic argon atmosphere was carried out to finally obtain the phosphorus functionalized graphene oxide, hereafter denoted as rGO800-P. For sake of comparison, reference reduced graphene

oxide samples were also prepared following the same route but in the absence of phosphoric acid (rGO800).

Activated carbon materials were prepared by a modified reported method.<sup>[23]</sup> Briefly, 440 mg of resorcinol (Sigma-Aldrich) were dissolved in 4.0 mL of water, 2.4 mL of ethanol and 4.0 mL of graphene oxide (4 mg mL<sup>-1</sup>). Then, 600 μL of formaldehyde and 100 μL of concentrated phosphoric acid were quickly added to the suspension and closed containers were transferred to an oven at 85 °C for 70 h. A subsequent pre-carbonization step was carried out at 800 °C in a tubular oven for 1 h under dynamic argon atmosphere. Then, carbon was grounded together with KOH in a mass ratio 1:6 and further heated in a tubular oven at 800 °C for 1 h under dynamic Ar atmosphere. Resulting material (ResFaGO-A) was washed once with a diluted solution of HCl and then several times with hot deionized water.

### Physicochemical Characterization

The morphological characterization was performed by Scanning Electron Microscopy (SEM) using a FEI Quanta250 microscope operating at 30 kV. Nitrogen adsorption-desorption isotherms at –196 °C were measured using ASAP 2460 instrument from Micromeritics. Samples were outgassed at 250 °C for 12 h under vacuum prior to the analysis. The specific surface area ( $S_{\text{BET}}$ ) was calculated according to the Brunauer-Emmett-Teller (BET) equation from the nitrogen isotherms. Raman spectra were recorded with a Rishaw spectrometer (Nanonics Multiview 2000) operating with an excitation wavelength of 523 nm. The microstructure of the samples was analyzed by X-ray diffraction (XRD) in a Bruker D8 X-ray diffractometer; data were collected using CuK $\alpha$  radiation over  $2\theta$  within the range from 10 to 80° at steps of 0.02°.

### Electrochemical Characterization

Both negative (rGO800 and rGO800-P) and positive (ResFaGO-A) electrodes were processed by mixing the active materials together with Super P C65 (Imerys Graphite & Carbon), and polyvinylidene fluoride (PVDF) in N-methyl-2-pyrrolidone (NMP) according to the 90:5:5 mass ratio. NMP-based inks of rGO800-P and ResFaGO-A were coated on copper and aluminium foil, respectively. Laminates were dried at 80 °C under vacuum overnight. Electrode discs of 11 mm in diameter were punched out and dried at 120 °C overnight under vacuum prior to the cell assembly.

rGO800 and rGO800-P were preliminarily evaluated in a half-cell configuration in a two-electrode Swagelok-type cell using a lithium disc as counter and reference electrode. The electrodes accounted with mass loadings of  $0.9 \pm 0.2$  mg cm<sup>-2</sup> and  $1.1 \pm 0.2$  mg cm<sup>-2</sup> for rGO800 and rGO800-P samples, respectively, with a corresponding thickness of  $75 \pm 20$  and  $90 \pm 20$  μm. Galvanostatic charge/discharge (GVs) measurements were carried at different C rates (being 1 C: 372 mAh g<sup>-1</sup> according to the theoretical capacity of graphite) between 0.002 and 2.0 V vs. Li/Li<sup>+</sup>. Electrochemical impedance spectroscopy (EIS) measurements were performed before and after lithiation using EL-cells, from 1 MHz to 10 mHz.

ResFaGO-A electrodes ( $1 \pm 0.5$  mg cm<sup>-2</sup>,  $200 \pm 20$  μm) were evaluated in a half-cell configuration in a three-electrode Swagelok-type cell using an oversized YP-80F (Kuraray) disc as counter electrode (10 mg cm<sup>-2</sup>) and a lithium disc as reference electrode. Galvanostatic charge/discharge (GVs) measurements and cyclic voltammeteries (CVs) were carried between 1.5 and 4.2 V vs. Li/Li<sup>+</sup>. AC-based electrodes were also evaluated as symmetric EDLCs using a two-electrode Swagelok-type cell. GV and CV measurements for EDLCs were performed within the 0–2.7 V cell voltage range.

Prior LIC cell assembly, rGO800-P electrode was pre-lithiated using a lithium metal disc. The pre-lithiation process involved 5 charge/discharge cycles at 0.1 C between 0.002 and 2.0 V vs. Li/Li<sup>+</sup>, followed by a final discharge to 0.2 V. Then, LICs were assembled using pre-lithiated rGO800-P as battery-type negative electrode vs. ResFaGO-A as capacitor-type positive electrode in a three-electrode Swagelok-type cell, using metallic lithium as reference electrode. Positive:negative electrode mass ratios of LIC 2:1 ( $1.3 \pm 0.2 \text{ mg cm}^{-2} : 0.8 \pm 0.2 \text{ mg cm}^{-2}$ ), LIC 1:1 ( $1.0 \pm 0.2 \text{ mg cm}^{-2} : 1.0 \pm 0.2 \text{ mg cm}^{-2}$ ), LIC 1:2 ( $1.0 \pm 0.2 \text{ mg cm}^{-2} : 2.0 \pm 0.2 \text{ mg cm}^{-2}$ ) and LIC 1:3 ( $1.0 \pm 0.2 \text{ mg cm}^{-2} : 3.0 \pm 0.2 \text{ mg cm}^{-2}$ ) were evaluated. Battery-type negative electrode potential was set to 0.2 V vs. Li/Li<sup>+</sup> and capacitor-type positive electrode to 4.2 V vs. Li/Li<sup>+</sup>. Galvanostatic charge/discharge measurements for the LICs were performed within the 1.5–4.2 V and 1.5–4.5 V cell voltage ranges at different current densities.

Whatman D-type glass fibres discs of 13 mm in diameter and 1 M LiPF<sub>6</sub> in 1:1 in volume of ethylene carbonate (EC) and dimethyl carbonate (DMC) were used as separator and electrolyte, respectively in all the measurements. Specific capacity, specific capacitance and current density values were calculated with respect to the total mass of active material.

## 2. Results and Discussion

### 2.1. Battery-Type Electrode

As described in the experimental section, reduced graphene oxide (rGO800) and P-functionalized graphene oxide (rGO800-

P) were selected as negative electrode materials for the lithium-ion capacitor. It is expected that graphene-based materials, specially functionalized ones, fasten the kinetics of the battery-type electrode on the final device, allowing a superior performance, especially at high current rates.<sup>[25–27]</sup> SEM images obtained for rGO800 (Figure 1a) show that the material is formed by graphene sheets that create a conductive network along the whole sample. It can be observed that the incorporation of phosphorus moieties leads to the restacking of some of these graphene sheets into dense agglomerates in rGO800-P sample (Figure 1b). The cavities between agglomerates are expected to serve as electrolyte reservoirs and improve the electrochemical performance of the sample, especially at high rates.<sup>[16]</sup>

To assess the impact of phosphorus on the textural properties, nitrogen adsorption/desorption isotherms were registered for both materials. rGO800 profile (Figure 1c) can be ascribed to a mixture of type II and IV with hysteresis loop H3 characteristic of macroporous adsorbents, while rGO800-P curve (Figure 1c) can be ascribed to a mixed type I and II with hysteresis loop H4 characteristic of micro-mesoporous carbons.<sup>[28]</sup> It is worth noticing that, the incorporation of phosphorus to the graphene matrix dramatically reduces the SSA from 76 to 22 m<sup>2</sup>g<sup>-1</sup> due to micropore clogging, as previously reported.<sup>[24]</sup>

Raman spectra were conducted to evaluate the distortions produced by the P-functionalization. The deconvolution of the Raman spectra (Figure 1d) of these materials shows two characteristic D and G bands at ca. 1345 and ca. 1593,

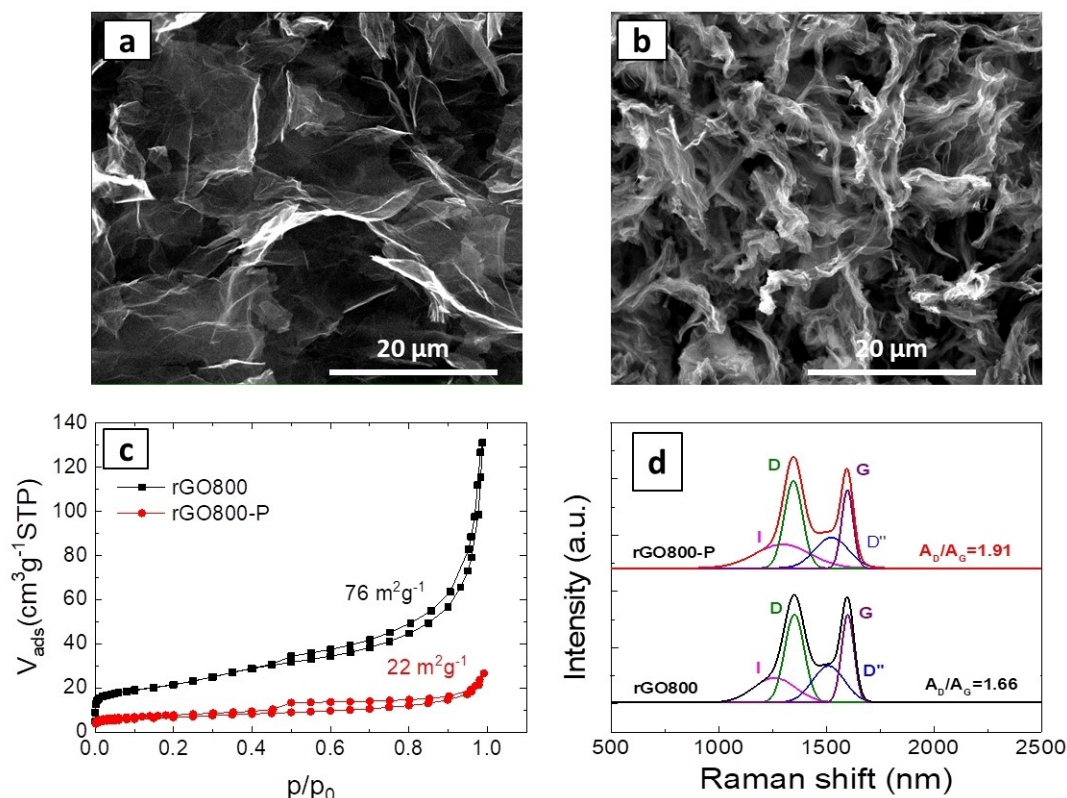


**Figure 1.** SEM images of rGO800 (a) and rGO800-P (b), nitrogen adsorption/desorption isotherms (c) and Raman spectra (d) for labelled samples.

respectively,<sup>[29]</sup> originated from the breathing mode of k-point phonons of the  $A_1^g$  symmetry and the first-order scattering of  $E_2^g$  phonons by the graphitic planes. These bands are related to the presence of structural defects in the graphene nanosheets and ordered graphitic domains, respectively. The larger areal ratio  $A_D/A_G$  measured for the rGO800-P (1.91) compared to the rGO800 (1.66) shows that the disordered degree is higher in the former sample and supports the incorporation of P-functional groups in the graphene matrix.<sup>[16,18,30]</sup> The fitted I band at ca. 1260 is normally attributed to the  $sp^2$ - $sp^3$  bonds, disorder in the graphitic lattice and the  $D''$  band at ca. 1550 is related to the presence of amorphous phases.<sup>[31–33]</sup>

The effect that the phosphate functionalization has on the crystallinity of these samples was evaluated by X-Ray diffraction (Figure S1). It can be observed a prominent and broad peak registered in the 20–30° range for both samples. This peak is indexed to the (002) peak, which is ascribed to the basal diffractions of graphene layers. It is centered at ca. 27° and 24°, for the rGO800 and rGO800-P, respectively. This shift towards lower  $2\theta$  values is related to the increase on the interlayered distances produced upon phosphate functionalization.<sup>[17]</sup> In addition, more randomly oriented graphene sheets, produce a widening of this peak in the pattern registered for the rGO800-P.<sup>[34]</sup> These results are in good agreement with the Raman results, which showed that graphene layers in rGO800-P are more disordered and showing larger interlayered distances than in the non-functionalized sample.

The atomic content of phosphorus in rGO800-P determined by energy dispersive X-ray spectroscopy (EDX) is 6%, which corresponds to 26% of phosphonate groups with C–P=O bond structure and 74% of phosphate-like groups with C–O–P=O bonding, as previously evidenced by NMR, XPS and FTIR analysis.<sup>[24]</sup>

The electrochemical performance of rGO800 and rGO800-P was initially evaluated in half-cell configuration in the potential range of 0.002–2.0 V (Figure 2). Galvanostatic charge/discharge profiles recorded for the first cycle (Figure 2a and 2b) evidences the strong impact of phosphorus over the formation of a stable solid electrolyte interphase (SEI).<sup>[35]</sup> It can be observed that the coulombic efficiency (C.E.) is highly improved from rGO800 (31%) to rGO800-P (64%). This reveals that the extent of irreversible reactions during the SEI formation is considerably reduced upon phosphorus functionalization. This result could be ascribed to a combination of the lower SSA of rGO800-P<sup>[15]</sup> and the presence of P moieties at the edge-planes sites, which could reduce the number of irreversible trapped lithium and fasten the electron transport along the sample.<sup>[18,36]</sup>

Galvanostatic charge/discharge curves at different rates for rGO800 and rGO800-P after 5 cycles of stabilization are depicted in Figure 2c and 2d, respectively. Both materials show similar sloping profiles characteristic of  $Li^+$  insertion in non-graphitic carbons with no marked plateaus.<sup>[37]</sup> The superior capacity performance of rGO800-P is clearly evidenced, delivering specific capacities as high as 461, 351, 316, 282 and 185  $mAh\ g^{-1}$  at current rates of C/10, C/2, C, 2C and 10 C respectively, with a coulombic efficiency close to 100% after the first activation cycle (Figure 2e). In contrast, rGO800 delivers

much lower capacities at similar current rates (252, 127, 97, 70 and 29  $mAh\ g^{-1}$ ) associated with a poor coulombic efficiency in the 10 first cycles. The outstanding capacity delivered by rGO800-P can be attributed to the active electron-donor type sites created by phosphorus that enhance the electronic conductivity and increase the interlayer distance favouring the  $Li^+$  intercalation.<sup>[16,18]</sup>

EIS analysis (Figure S2) supports the better electrochemical performance exhibited by the phosphate-functionalized sample. Before lithiation (Figure S2a) its resistance is 3 times lower than that measured for the rGO800, evidencing its better electronic conductivity, and the lower charge transfer resistance measured for the rGO800-P sample after lithiation (Figure S2b), indicates a faster lithium ion diffusion through the SEI layer and the electrode/electrolyte interface.<sup>[26]</sup>

## 2.2. Capacitor-Type Electrode

As mentioned above, activated carbons are the preferred choice for capacitive-type electrodes in lithium-ion capacitors.<sup>[9]</sup> Herein, ResFaGO-A prepared by the condensation and activation of a phenolic resin in the presence of graphene has been used as positive electrode in the final LIC.

SEM image of ResFaGO-A is depicted on Figure 3a. As previously reported,<sup>[23]</sup> graphene sheets act as templates for resorcinol formaldehyde condensation, resulting in a flat-shaped morphology due to the homogeneously covering of graphene sheets by the activated carbon particles. This morphology is expected to help the ions diffusion into the porous structure, promoting the double-layer formation, even at high current densities.

The nitrogen adsorption/desorption isotherm of ResFaGO-A shows a profile (Figure 3b) that corresponds to type-I, according to IUPAC classification, which is characteristic of microporous materials.<sup>[28]</sup> The slight increase on nitrogen adsorption at high relative pressures reveals the presence of large interparticle mesopores.<sup>[23]</sup> According to the BET calculations ResFaGO-A exhibits a SSA of 2318  $m^2\ g^{-1}$  and contains a wide pore size distribution (Figure 3b-inset), which covers all the microporous range from ultramicropores (0.59 nm) to large micropores (1.85 nm).

The electrochemical performance of the activated composite ResFaGO-A as positive electrode was investigated in the potential range 1.5–4.2 V vs  $Li/Li^+$  in three-electrode configuration. Almost rectangular shaped CV curves were registered at different sweep rates (Figure 4a), which are typically reported for samples undergoing capacitive-type charge storage mechanism. The large SSA and wide pore size distribution combined with the presence of graphene account for its high specific capacitance 181  $F\ g^{-1}$  (136  $mAh\ g^{-1}$ ) measured at 0.25  $A\ g^{-1}$  and excellent capacitance retention 84  $F\ g^{-1}$  (60  $mAh\ g^{-1}$ ) at 40  $A\ g^{-1}$  (Figure 4b).<sup>[38]</sup>

For the sake of comparison, a symmetric EDLC cell was also assembled and tested in a voltage range of 0–2.7 V. Figure 4c and 4d further confirm the good capacitance performance of this material. Both CV profiles and the evolution of the specific

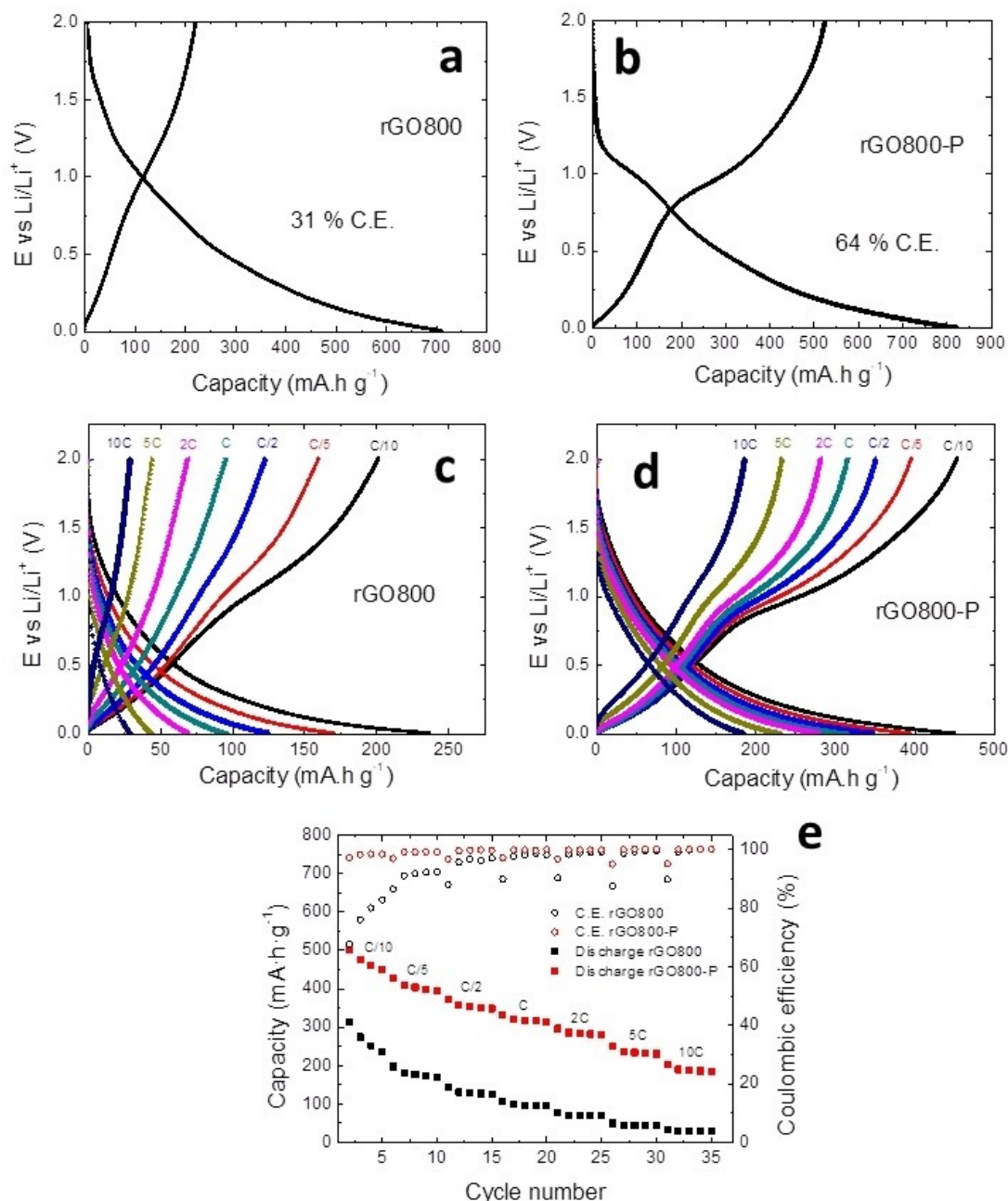


**Figure 2.** Electrochemical characterization of the battery-type electrodes: Galvanostatic charge/discharge curves for the first cycle and at different current rates for rGO800 (a) and (c) and for rGO800-P (b) and (d) respectively and rate capability and their respective coulombic efficiency (e)

capacitance with the current density are in good agreement with the results obtained in three-electrode configuration.

### 2.3. Lithium-Ion Capacitor

As previously discussed, different storage mechanisms can take place on each electrode, and consequently, electrode materials have to be carefully chosen and optimized. For this reason, ResFaGO-A, an activated carbon with a large SSA and high capacitance, was selected as the positive electrode. On the

other hand, rGO800-P was chosen as battery-type electrode due to its ability to reversibly accommodate a large amount of lithium into the structure leading to excellent coulombic efficiencies in the first cycles and good electrochemical performance, especially at high rates. Prior the LIC assembly, the rGO800-P electrode was cycled five times between 0.002 and 2 V vs Li/Li<sup>+</sup> at C/10 rate using an auxiliary Li electrode in order to form a SEI and supply enough lithium and to balance the first cycles irreversibility. Then, a cut-off potential of 0.2 V vs Li/Li<sup>+</sup> was set to maximize the use of the negative electrode while preventing lithium plating in the full cell.

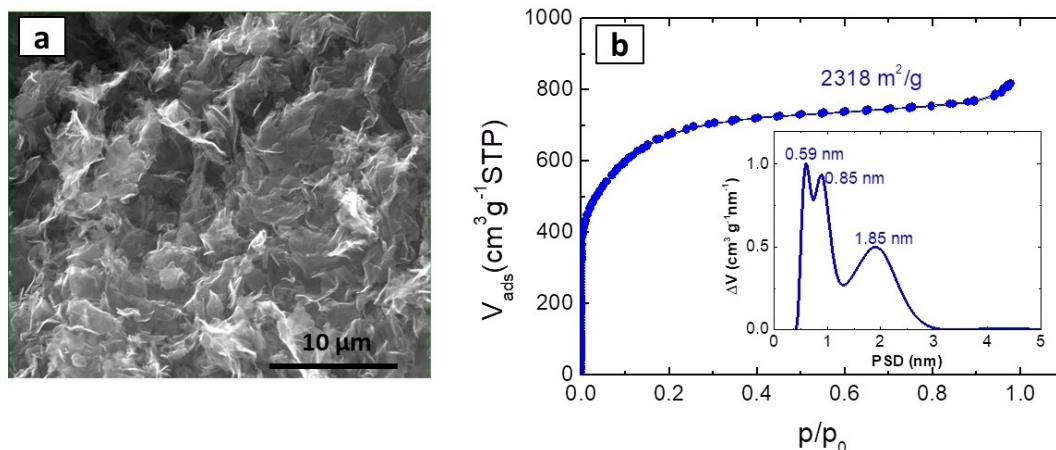


Figure 3. SEM image (a) and nitrogen adsorption/desorption isotherm (inset: pore size distribution) (b) of ResFaGO-A

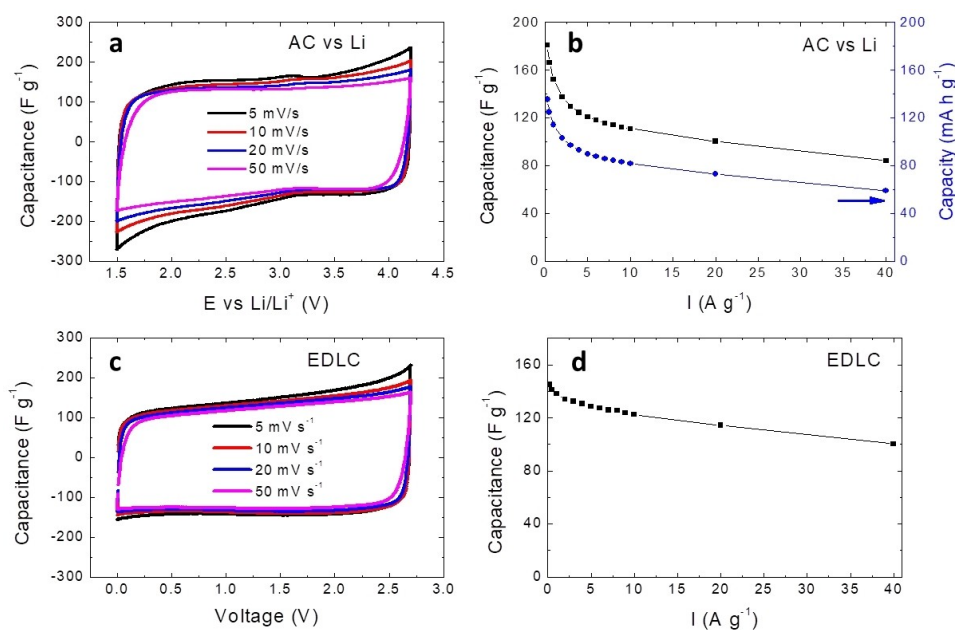


Figure 4. Electrochemical characterization of the capacitor-type electrode ResFaGO-A: Cyclic voltammograms (a) and dependence of the specific capacitance/capacity with the current density (b) in three-electrode cell configuration and cyclic voltammograms (c) and dependence of the specific capacitance with the current density (d) in two-electrode cell configuration.

With the aim of maximizing the output capacity, mass balance of the electrodes was performed.<sup>[39–41]</sup> In this regard, the charge stored in both electrodes must be equal  $Q_+ = Q_-$  and it is influenced by the specific capacitance of each electrode ( $C_+$ ,  $C_-$ ), the active mass of the electrode materials ( $m_+$ ,  $m_-$ ) and the working potential window ( $\Delta E_+$ ,  $\Delta E_-$ ) [Eqs. (1) and (2)].

$$Q_+ = m_+ C_+ \Delta E_+ \quad (1)$$

$$Q_- = m_- C_- \Delta E_- \quad (2)$$

Since the capacity of both electrodes diverges along the applied current rates (Figure S3a), it is difficult to find a unique

mass ratio that can maximize energy and power density in the whole current range. Thus, various LICs showing the mass ratios LIC 2:1, LIC 1:1 and LIC 1:2 (being LIC  $m_+ : m_-$ ) were investigated.

LICs were galvanostatically cycled at different current densities in the 1.5–4.2 V cell voltage range (Figure 5). At  $0.5 \text{ A g}^{-1}$  the profiles of the full LICs are almost symmetric showing a linear voltage increase/decrease during the charge/discharge, which is typical of capacitive storage.<sup>[4]</sup> It is observed that for LIC 2:1 (Figure 5a), when time discharge corresponds to 3.5 min ( $0.5 \text{ A g}^{-1}$ ) the positive electrode potential swings from 2.6 to 4.3 V (1.7 V) while the negative electrode fluctuates from 0.1 to 1.1 V (1.0 V). In the case of the LIC 1:1 (Figure 5b), for a discharge time close to 3.5 min, the positive electrode

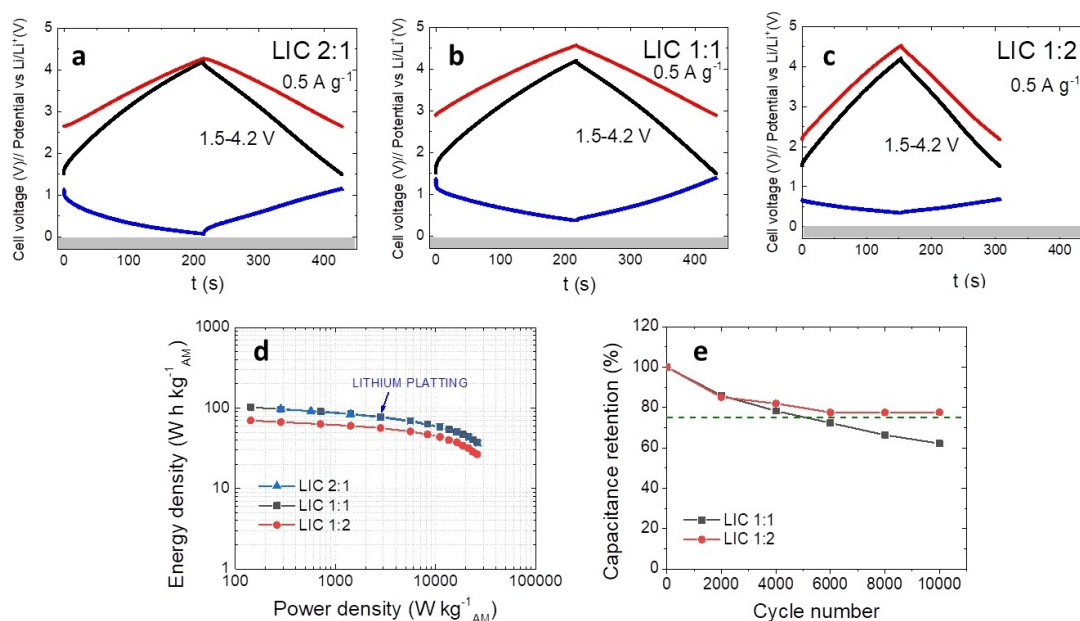


**Figure 5.** Galvanostatic charge/discharge profiles registered at  $0.5 \text{ A g}^{-1}$  in the cell voltage 1.5–4.2 V for LIC 2:1 (a), LIC 1:1 (b) and LIC 1:2 (c): LIC (black), positive electrode (red) and negative electrode (blue). Ragone plot comparing LIC 2:1 LIC 1:1 and LIC 1:2 (c) and cycling performance of LIC 1:1 and LIC 1:2 at  $5 \text{ A g}^{-1}$  (e)

potential swings from 2.9 to 4.6 V (1.7 V) and the negative electrode fluctuates from 0.4 to 1.4 V (1.0 V). Finally, for LIC 1:2 (Figure 5c), for a slightly faster discharge time of 2.5 min, the positive electrode potential swings from 2.2 to 4.5 V (2.3 V) and the negative electrode only fluctuates within the 0.3–0.7 V range (0.4 V). It seems that as the mass of the positive electrode is increased, the potential window of the negative electrode is extended to balance the charge, which results in a capacitance improvement of the LIC cell (Figure S3b). Nevertheless, the extension in the potential window of the negative electrode can lead to lithium plating at high current rates which can compromise the cell safety.<sup>[42]</sup> This fact is clearly evidenced for LIC 2:1 (Figure S4a), where lithium plating occurs for current densities above  $4 \text{ A g}^{-1}$ .

The energy and power density evolution of the LICs calculated from the GV curves in the voltage range 1.5–4.2 V are included in Figure 5d. It can be observed that LIC 1:1 and LIC 2:1 deliver similar energy values in the whole power range, both of them outperforming the values measured for LIC 1:2. However, LIC 2:1 undergoes lithium plating at the early  $3000 \text{ W kg}^{-1}$  which can decrease its cyclability and seriously damage the cell safety.

So, taking into account all these issues LIC 2:1 was discarded while LIC 1:1 and LIC 1:2 were further cycled for 10,000 charge/discharge cycles at  $5 \text{ A g}^{-1}$ . The poor cycling performance of LIC 1:1 compared to LIC 1:2 is evidenced in Figure 5e. LIC 1:1 reaches the 75% of its initial capacitance (green line) after 5,000 cycles, whereas LIC 1:2 still shows 78% after 10,000 cycles. It seems that oversizing the negative electrode mass leads to lower energy and power values but prevents cell degradation and extends cycle life.

A different strategy to improve the energy density of the LIC consists of widening the voltage window of the cell.<sup>[6]</sup> However, voltage extension generally favors some parasitic reactions and the electrolyte decomposition that could eventually shorten the cycle life of the cell. In addition, the risk of lithium plating is enhanced when the voltage window is extended due to the strong potential fluctuations taking place in the negative electrode.<sup>[43]</sup> However, taking into account our previous results, oversizing the negative electrode seems to be an effective way to overcome these issues. Thus, a LIC with a mass balance 1:3 was assembled and firstly tested within the 1.5–4.2 V cell voltage range. Since there were no evidences of lithium plating nor electrolyte degradation (Figure S5), the cell voltage was further extended to 1.5–4.5 V. Figure S6 shows GVs profiles at  $0.5 \text{ A g}^{-1}$  of LIC 1:3 in the cell voltage 1.5–4.2 V and 1.5–4.5 V. Both profiles display typical triangular shape curves discarding the contribution of any faradaic reaction in this voltage range, and supporting the good stability of the electrolyte.<sup>[44]</sup>

The contribution of each electrode to the full cell in the extended cell voltage 1.5–4.5 V are shown in Figure 6. At the low current density  $0.5 \text{ A g}^{-1}$  (Figure 6a), within a discharge time of 3.1 min, the positive electrode potential swings from 1.9 to 4.8 V (2.9 V) and the negative electrode only fluctuates from 0.4 to 0.3 V (0.1 V). When the current density is increased up to  $5 \text{ A g}^{-1}$  (Figure 6b), with an associated discharge time of 13 s, the potentials of both positive and negative electrodes remain unchanged. This means that, although the contribution of the negative electrode to the total capacitance of the LIC is almost negligible it ensures high voltage operation under safe conditions.

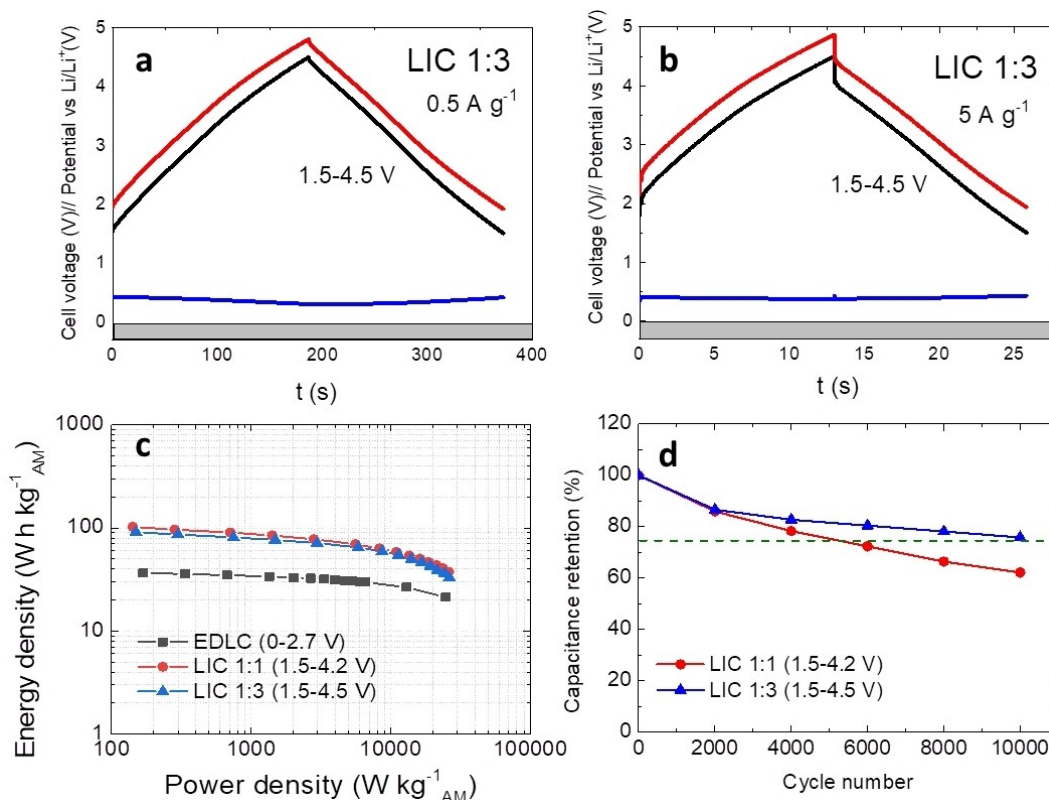


**Figure 6.** Galvanostatic charge/discharge profiles of LIC 1:3 registered at  $0.5 \text{ A g}^{-1}$  (a) and  $5 \text{ A g}^{-1}$  (b) in the cell voltage 1.5–4.5 V: LIC (black), positive electrode (red) and negative electrode (blue). Ragone plot comparing symmetric EDLC, LIC 1:1 and LIC 1:3 (c) and cycling performance of LIC 1:1 and LIC 1:3 at  $5 \text{ A g}^{-1}$  (d)

The small increase of 0.3 V in the cell voltage of LIC 1:3 has a strong impact on the energy and power densities (Figure 6c).<sup>[45]</sup> It can be observed that for a similar power rate LIC 1:1 and LIC 1:3 deliver similar energy densities, largely improving their EDLC counterpart. The electrochemical stability of LIC 1:3 in the high cell voltage 1.5–4.5 V was tested by GV charge/discharge at  $5 \text{ A g}^{-1}$  and compared with that of LIC 1:1 in the cell voltage 1.5–4.2 V (Figure 6d). After 10,000 cycles LIC 1:3 with 76% capacitance retention clearly outperform LIC 1:1 with 62% capacitance retention. Hence, increasing the mass loading of the negative electrode enabled moderate energy and high power performance together with excellent cycling stability. To the best of our knowledge the cycling and power performance of LIC 1:3 surpasses most of graphene-based LICs reported so far in the state of the art, as summarized in Table 1.

### 3. Conclusions

The potential use of P-functionalized graphene as battery-type electrode in LICs technology has been demonstrated. Specifically, it was found that the incorporation of phosphorus functional groups into the graphene layers improved the coulombic efficiency of the first cycle from 31% to 64%, the specific capacity at C/10 from 252 to  $461 \text{ mAh g}^{-1}$  and at 10 C from 29 to  $185 \text{ mAh g}^{-1}$ .

The suitable flat shaped morphology, high specific surface area and wide pore size distribution of the graphene-based composite used as capacitor-type electrode led to capacitance values of  $182 \text{ F g}^{-1}$  at  $0.25 \text{ A g}^{-1}$  and  $84 \text{ F g}^{-1}$  at  $40 \text{ A g}^{-1}$ .

Moreover, it was demonstrated that a further optimization of the LIC assembly, based on the oversizing of the negative electrode, allowed widening the cell voltage up to 1.5–4.5 V under safe operating conditions, showing an energy density of  $91 \text{ Wh kg}^{-1}_{\text{AM}}$  at the power density of  $145 \text{ W kg}^{-1}_{\text{AM}}$  and retaining  $33 \text{ Wh kg}^{-1}_{\text{AM}}$  at  $26000 \text{ W kg}^{-1}_{\text{AM}}$ . Furthermore, this device delivered exceptional capacitance retention of 76% after 10,000 cycles.

### Acknowledgements

The authors thank the European Union (Graphene Flagship, Core 3, Grant number 881603) and the Spanish Ministry of Science and Innovation (MICINN/FEDER) (RTI2018-096199-B-I00) for the financial support of this work. J. L. G. U. is very thankful to the Spanish Ministry of Education, Science and Universities (MICINN) for the FPU grant (16/03498). We also want to acknowledge the company GRAPHENEA for supplying the graphene oxide used in this work.

**Table 1.** Electrochemical performance of representative graphene-based lithium ion capacitors

Positive electrode	SSA [m <sup>2</sup> g <sup>-1</sup> ]	Positive electrode capacity [mAhg <sup>-1</sup> ]	Negative electrode	Negative electrode capacity [mAhg <sup>-1</sup> ]	LIC voltage window [V]	LIC maximum power density [Wh kg <sup>-1</sup> ]	Number of cycles [% Retention]	Ref.
3D Activated N-doped graphene	2225	110 at 0.1 A g <sup>-1</sup>	3D N-doped graphene	400 at 0.1 A g <sup>-1</sup>	2–4.5	11250	3000 (93%)	[13]
AC from olive pits Graphene@hierarchical meso-microporous carbon	2675	112 at 0.2 A g <sup>-1</sup>	HC from olive pits/rGO	400 at 0.1 A g <sup>-1</sup>	1.0–4.2	23000	10000 (85%)	[26]
Porous 3D graphene-based carbon	3523	110 at 0.1 A g <sup>-1</sup>	Self-standing Flash reduced graphene oxide	660 at 0.75 A g <sup>-1</sup>	2–4.5	15700	3000 (90%)	[46]
N-doped hierarchical carbon nanolayer SWCNT/rGO	2350	125 at 0.5 A g <sup>-1</sup>	Mesoporous graphene SWCNT/rGO	884 at 0.093 A g <sup>-1</sup> 500 at 0.05 A g <sup>-1</sup>	0–4.2	7000	3000 (65%)	[47]
AC KOH activated coffee waste KOH activated graphene/carbon composite	2350 2318	65 at 0.1 A g <sup>-1</sup> 150 at 0.1 A g <sup>-1</sup> 136 at 0.25 A g <sup>-1</sup>	N-rGO/r-MWCNTO Coffee waste derived carbon P-functionalized reduced graphene oxide	1754 at 0.1 A g <sup>-1</sup> 398 at 0.186 A g <sup>-1</sup> 316 at 0.372 A g <sup>-1</sup>	2–4 1.5–4.2 1.5–4.5	24105 15000 26000	7000 (54%) 3000 (80%) 10,000 (76%)	[15] [50] <b>This work</b>

## Conflict of Interest

The authors declare no conflict of interest.

**Keywords:** activated carbon · long stability · metal-ion hybrid capacitors · phosphorus functionalization · supercapacitor

- [1] C. M. Hayner, X. Zhao, H. H. Kung, *Annu. Rev. Chem. Biomol. Eng.* **2012**, *3*, 445–471.
- [2] V. Etacheri, R. Marom, R. Elazari, G. Salitra, D. Aurbach, *Energy Environ. Sci.* **2011**, *4*, 3243.
- [3] N. Nitta, F. Wu, J. T. Lee, G. Yushin, *Mater. Today* **2015**, *18*, 252–264.
- [4] R. Holze, *J. Solid State Electrochem.* **2015**, *19*, 1253–1253.
- [5] A. González, E. Goikolea, J. A. Barrena, R. Mysyk, *Renewable Sustainable Energy Rev.* **2016**, *58*, 1189–1206.
- [6] G. Li, Z. Yang, Z. Yin, H. Guo, Z. Wang, G. Yan, Y. Liu, L. Li, J. Wang, *J. Mater. Chem. A* **2019**, *7*, 15541–15563.
- [7] J. Ding, W. Hu, E. Paek, D. Mitlin, *Chem. Rev.* **2018**, *118*, 6457–6498.
- [8] X. Sun, W. Chen, X. Li, J. Wang, H. Hu, G. Liang, Y. Huang, C. Wei, in *Sci. Technol. Adv. Appl. Supercapacitors* (Ed.: T. Sato), IntechOpen, **2019**.
- [9] X. Wang, L. Liu, Z. Niu, *Mater. Chem. Front.* **2019**, *3*, 1265–1279.
- [10] S. S. Zhang, *Batteries Supercaps* **2020**, *3*, 1137–1146.
- [11] C. Li, X. Zhang, C. Sun, K. Wang, X. Sun, Y. Ma, *J. Phys. Appl. Phys.* **2019**, *52*, 143001.
- [12] B. Babu, P. Simon, A. Balducci, *Adv. Energy Mater.* **2020**, 2001128.
- [13] R. Wang, Q. Zhao, W. Zheng, Z. Ren, X. Hu, J. Li, L. Lu, N. Hu, J. Molenda, X. Liu, C. Xu, *J. Mater. Chem. A* **2019**, *7*, 19909–19921.
- [14] J. H. Lee, W. H. Shin, M.-H. Ryou, J. K. Jin, J. Kim, J. W. Choi, *ChemSusChem* **2012**, *5*, 2328–2333.
- [15] C. Aphirakaramwong, N. Phattharasupakun, P. Suktha, A. Krittayavathananon, M. Sawangphruk, *J. Electrochem. Soc.* **2019**, *166*, A532–A538.
- [16] C. Zhang, N. Mahmood, H. Yin, F. Liu, Y. Hou, *Adv. Mater.* **2013**, *25*, 4932–4937.
- [17] Y. Zhu, Y. Huang, C. Chen, M. Wang, P. Liu, *Electrochim. Acta* **2019**, *321*, 134698.
- [18] C. Ma, C. Deng, X. Liao, Y. He, Z. Ma, H. Xiong, *ACS Appl. Mater. Interfaces* **2018**, *10*, 36969–36975.
- [19] Z. Yu, J. Song, M. L. Gordin, R. Yi, D. Tang, D. Wang, *Adv. Sci.* **2015**, *7*.
- [20] Z. Lin, E. Goikolea, A. Balducci, K. Naoi, P. L. Taberna, M. Salanne, G. Yushin, P. Simon, *Mater. Today* **2018**, *21*, 419–436.
- [21] J. Guo, D. Wu, T. Wang, Y. Ma, *Appl. Surf. Sci.* **2019**, *475*, 56–66.
- [22] J. Zhou, Z. Qiu, J. Zhou, W. Si, H. Cui, S. Zhuo, *Electrochim. Acta* **2015**, *180*, 1007–1013.
- [23] G. Moreno-Fernández, J. L. Gómez-Urbano, M. Enterría, T. Rojo, D. Carriazo, *J. Mater. Chem. A* **2019**, *7*, 14646–14655.
- [24] G. Moreno-Fernández, J. L. Gómez-Urbano, M. Enterría, R. Cid, J. M. López del Amo, R. Mysyk, D. Carriazo, *Electrochim. Acta* **2020**, *361*, 136985.
- [25] Y. Ma, H. Chang, M. Zhang, Y. Chen, *Adv. Mater.* **2015**, *27*, 5296–5308.
- [26] J. Ajouria, M. Zarrabeitia, M. Arnaiz, O. Urrea, T. Rojo, E. Goikolea, *J. Electrochem. Soc.* **2019**, *166*, A2840–A2848.
- [27] Z.-S. Wu, W. Ren, L. Xu, F. Li, H.-M. Cheng, *ACS Nano* **2011**, *5*, 5463–5471.
- [28] M. Thommes, K. Kaneko, A. V. Neimark, J. P. Olivier, F. Rodriguez-Reinoso, J. Rouquerol, K. S. W. Sing, *Pure Appl. Chem.* **2015**, *87*, 1051–1069.
- [29] J.-B. Wu, M.-L. Lin, X. Cong, H.-N. Liu, P.-H. Tan, *Chem. Soc. Rev.* **2018**, *47*, 1822–1873.
- [30] X. Mu, B. Yuan, X. Feng, S. Qiu, L. Song, Y. Hu, *RSC Adv.* **2016**, *6*, 105021–105029.
- [31] L. Hou, Z. Chen, Z. Zhao, X. Sun, J. Zhang, C. Yuan, *ACS Appl. Mater. Interfaces* **2019**, *2*, 548–557.
- [32] K. Tan, Y. Liu, Z. Tan, J. Zhang, L. Hou, C. Yuan, *J. Mater. Chem. A* **2020**, *8*, 3048–3059.
- [33] D. López-Díaz, M. López Holgado, J. L. García-Fierro, M. M. Velázquez, *J. Phys. Chem. C* **2017**, *121*, 20489–20497.
- [34] S. H. Huh, in *Phys. Appl. Graphene* (Ed.: S. Mikhailov), IntechOpen, Rijeka, **2011**.
- [35] X. Liu, D. Teng, T. Li, Y. Yu, X. Shao, X. Yang, *J. Power Sources* **2014**, *272*, 614–621.

- [36] N. Phattharasupakun, J. Wutthiprom, P. Suktha, N. Ma, M. Sawangphruk, *J. Electrochem. Soc.* **2018**, *165*, A609–A617.
- [37] B. N. Loeffler, D. Bresser, S. Passerini, M. Copley, *Johns. Matthey Technol. Rev.* **2015**, *59*, 34–44.
- [38] R. Härmas, R. Palm, M. Härmas, M. Pohl, H. Kurig, I. Tallo, E. Tee, I. Vaas, R. Väli, T. Romann, O. Oll, R. Kanarbik, K. Liivand, J. Eskusson, J. Kruusma, T. Thomberg, A. Jänes, P. Miidla, E. Lust, *Electrochim. Acta* **2018**, *283*, 931–948.
- [39] S. Dsoke, B. Fuchs, E. Gucciardi, M. Wohlfahrt-Mehrens, *J. Power Sources* **2015**, *282*, 385–393.
- [40] M. Arnaiz, J. L. Gómez-Cámer, F. Mijangos, T. Rojo, E. Goikolea, J. Ajuria, *Batteries Supercaps* **2019**, *2*, 153–159.
- [41] G. Madabattula, B. Wu, M. Marinescu, G. Offer, *J. Electrochem. Soc.* **2020**, *167*, 013527.
- [42] Q. Liu, C. Du, B. Shen, P. Zuo, X. Cheng, Y. Ma, G. Yin, Y. Gao, *RSC Adv.* **2016**, *6*, 88683–88700.
- [43] M. R. Lukatskaya, B. Dunn, Y. Gogotsi, *Nat. Commun.* **2016**, *7*, 12647.
- [44] A. Krause, A. Balducci, *Electrochem. Commun.* **2011**, *13*, 814–817.
- [45] M. Arnaiz, E. Goikolea, T. Rojo, L. Wittscher, A. Balducci, J. Ajuria, *J. Power Sources* **2019**, *434*, 226757.
- [46] N.-W. Li, X. Du, J.-L. Shi, X. Zhang, W. Fan, J. Wang, S. Zhao, Y. Liu, W. Xu, M. Li, Y.-G. Guo, C. Li, *Electrochim. Acta* **2018**, *281*, 459–465.
- [47] T. Zhang, F. Zhang, L. Zhang, Y. Lu, Y. Zhang, X. Yang, Y. Ma, Y. Huang, *Carbon* **2015**, *92*, 106–118.
- [48] C. Li, X. Zhang, K. Wang, X. Sun, Y. Ma, *Carbon* **2018**, *140*, 237–248.
- [49] Y. Sun, J. Tang, F. Qin, J. Yuan, K. Zhang, J. Li, D.-M. Zhu, L.-C. Qin, *J. Mater. Chem. A* **2017**, *5*, 13601–13609.
- [50] J. L. Gómez-Urbano, G. Moreno-Fernández, M. Arnaiz, J. Ajuria, T. Rojo, D. Carriazo, *Carbon* **2020**, *162*, 273–282.

---

Manuscript received: October 19, 2020  
Revised manuscript received: November 19, 2020  
Accepted manuscript online: November 30, 2020  
Version of record online: December 14, 2020